Journal of Colloid and Interface Science 678 (2025) 873–885

Contents lists available at ScienceDirect

Journal of Colloid And Interface Science

journal homepage: www.elsevier.com/locate/jcis

Regular Article

Hydrophobic iron oxide nanoparticles: Controlled synthesis and phase transfer via flash nanoprecipitation

Sulalit Bandyopadhyay [a,*,1], Haroon Zafar [a,1], Muhammad Sarmad Khan [a], Reema Ansar [a], Davide Peddis [b,c], Sawssen Slimani [b,c], Nesrine Bali [a], Zahra Sajid [d], Rida e Maria Qazi [d], Fawad ur Rehman [d], Afsar Ali Mian [d]

[a] Particle Engineering Centre, Department of Chemical Engineering, Norwegian University of Science and Technology, NTNU, Trondheim, 7491, Norway
[b] Istituto di Struttura Della Materia, ISM-CNR, Università di Genova, 00015, Monterotondo Scalo, RM, Italy
[c] Dipartimento di Chimica e Chimica Industriale, Università di Genova, I-16146, Genova, Italy
[d] Centre for Regenerative Medicine and Stem Cells Research, The Aga Khan University, Karachi, Pakistan

GRAPHICAL ABSTRACT

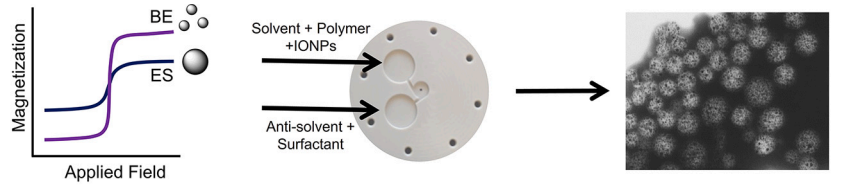

ARTICLE INFO

Keywords:
Iron oxide nanoparticles
Flash nanoprecipitation
Phase transfer
Thermal decomposition
Polymer coating
Encapsulation
Functionalization

ABSTRACT

Iron oxide nanoparticles (IONPs) synthesized via thermal decomposition find diverse applications in biomedicine owing to precise control of their physico-chemical properties. However, use in such applications requires phase transfer from organic solvent to water, which remains a bottleneck.

Through the thermal decomposition of iron oleate (FeOl), we systematically investigate the impact of synthesis conditions such as oleic acid (OA) amount, temperature increase rate, dwell time, and solvent on the size, magnetic saturation, and crystallinity of IONPs. Solvent choice significantly influences these properties, manipulating which, synthesis of monodisperse IONPs within a tunable size range (10-30 nm) and magnetic properties (75 to 42 Am^2Kg^{-1}) is obtained.

To enable phase transfer of IONPs, we employ flash nanoprecipitation (FNP) for the first time as a method for scalable and precise size control, demonstrating its potential over conventional methods. Poly(lactic-co-glycolic acid) (PLGA)-coated IONPs with hydrodynamic diameter (H_d) in the range of 250 nm, high colloidal stability and high IONPs loadings up to 43% were obtained, such physicochemical properties being tuned exclusively by the size and hydrophobicity of starting IONPs. They showed no discernible cytotoxicity in human dermal fibroblasts, highlighting the applicability of FNP as a novel method for the functionalization of hydrophobic IONPs for biomedicine.

* Corresponding author.
E-mail address: sulalit.bandyopadhyay@ntnu.no (S. Bandyopadhyay).
[1] Both authors contributed equally.

https://doi.org/10.1016/j.jcis.2024.09.134
Received 21 May 2024; Received in revised form 11 September 2024; Accepted 14 September 2024
Available online 19 September 2024

1. Inroduction

The field of bio-medicine has been revolutionized by IONPs owing to their superparamagnetic properties and easy surface tailoring for a plethora of applications ranging from diagnostics [1,2] to therapeutics [3] such as magnetic hyperthermia and targeted drug delivery, etc. [4–6] Their performance in such applications is governed by their magnetic properties which in turn are influenced by particle size, shape, interparticle interactions among others, necessitating the need to correlate synthesis conditions to physico-chemical properties.

Thermal decomposition of precursors like FeOl and iron pentacarbonyl in organic solvents offers precise control over the size, size distribution, and magnetic properties of IONPs in comparison to co-precipitation methods. [7–9] The resultant nanoparticles (NPs) properties are influenced by a complex interplay of the reaction temperature, [10] precursor-to-ligand ratio, reflux time, [8] solvent nature, [11] etc. Octadecene (ODE), a commonly used solvent in the thermal decomposition of FeOl, facilitates size control but often compromises the magnetic properties of synthesized IONPs due to the formation of reduced and non-magnetic wüstite phases resulting from solvent degradation at elevated temperatures. [12] Other solvents such as eicosane (ES), and benzyl ether (BE) have been reported in the literature, however, there exists no study to our knowledge where a systematic investigation of the solvent effect on IONPs properties has been reported.

A major drawback of the thermal decomposition is that the IONPs remain dispersed in an organic solvent, limiting their applications within biomedicine. This necessitates an additional phase transfer step which could be based on oxidative cleavage, ligand exchange, binding of amphiphilic molecules as a surfactant, etc. [13–15]. Phase transfer also introduces other caveats such as aggregation, reduction in magnetic properties, change in surface properties, and so on. Further functionalization may be required to impart specific properties to the IONPs, such as colloidal stability, stimuli sensitivity, etc., for which several works resort to the use of polymers that are either grown *in situ* grafted to/from the IONPs surfaces it assembled chemically, [16,17] leading to complicated downstream processing prior to applications.

FNP has gained remarkable attention since it can be used to encapsulate hydrophobic components such as drugs within amphiphilic polymers besides other operational advantages such as scalability, robustness in terms of applicability to a large portfolio of materials, continuous operation, and so on. The process of formation of such polymeric nanoparticles (PNPs) relies on rapid micro-mixing of two miscible liquid streams: the organic stream containing a molecularly dissolved hydrophobic compound and amphiphilic molecule and the aqueous stream containing a surfactant/stabilizer. [18,19] Tween 80 (polysorbate 80) is a widely used non-ionic surfactant in FNP, particularly for its ability to stabilize nanoparticles by providing steric stabilization. The polyoxyethylene chains of Tween 80 extend into the aqueous phase, creating a physical barrier that prevents nanoparticles from coming into close contact. [20] The contents of the organic stream precipitate out upon mixing with the aqueous phase, thus making the mixing process a crucial step in controlling particle size and size distribution - the mixing time scale must be shorter than the time required for nanoparticle formation via nucleation, growth, and aggregation. [19] Such turbulent mixing is achieved in practice either through a confined impinging jet mixer or a multi-inlet vortex mixer. [21] Particle size in FNP can be further tuned by changing supersaturation levels via, for example, the solute solubility in the mixed solvent, the organic solvent to water ratio, the amount and nature of the stabilizer, and the chemical structure and molecular weight of the polymer. [18]

Herein, we report for the first time how one can leverage the advantages of the FNP process using a multi-inlet vortex mixer to functionalize IONPs synthesized via thermal decomposition. Our methodology serves a dual purpose: (i) facilitating the phase transfer of hydrophobic IONPs and (ii) enabling polymer encapsulation of the IONPs, leading to magnetically tunable PNPs. In the first part, through systematic investigation of synthesis conditions, including solvent type, ligand quantity, temperature ramp rate, and dwell time, we elucidate their impact on the physico-chemical properties of IONPs. Subsequently, we demonstrate, for the first time, the encapsulation of representative IONPs within PLGA spheres using optimized FNP conditions. Finally, we evaluate the influence of the functionalization process on the physicochemical properties of the IONPs and their interactions with selected cell lines to assess biocompatibility.

2. Materials and methods

2.1. Materials

Sodium Oleate, 97% was purchased from TCI Chemicals, Ethanol, ≥ 96%, Acetone, ≥ 99%, 2-Propanol, ≥ 98% - technical were purchased from VWR, while Iron (III) Chloride Hexahydrate, ≥ 99%, Hexane, 95% - anhydrous, 1-Octadecene, 90% - technical, Oleic Acid, 90% – Technical, Toluene, 99.8% - anhydrous, Benzyl Ether, 98%, n - Eicosane, ≥ 98%, Tetrahydrofuran, ≥ 99.9%, Resomer® RG 503, Poly(D, L-lactide-co-glycolide) ester terminated with lactide: glycolide ratio 50:50, molecular weight 24 - 38 kDa and Tween 80 were purchased from Sigma Aldrich. PLGA, molecular weight 24 - 38 kDa was purchased from BLD Pharmatech Ltd and delivered by VWR. All chemicals were used as received. Milli-Q water having a resistivity of 18.2 MΩ-cm at 25 °C, produced by the Sartorius Arium mini Water System, was used for all experiments. Cell culture media, Dulbecco's Modified Eagle Medium (DMEM), and supplements were purchased from Gibco Inc. Billings, MT, USA. Cell culture plasticware was obtained from ThermoFisher Scientific (Waltham, MA, USA) unless otherwise mentioned. XTT assay reagents (XTT Cell Proliferation Kit II) were purchased from Roche (Switzerland). Annexin-V was purchased from BD Bioscience (New Jersey, US), and propidium iodide (PI) was obtained from Invitrogen, ThermoFisher Scientific (Waltham, MA, USA).

2.2. Methods

2.2.1. Synthesis of iron oleate

FeOl was synthesized following our previous work. [22] In a 250 ml single-necked round bottom flask, a mixture consisting of 25 ml of MQ water, 70 ml of hexane, and 40 ml of ethanol was stirred at 1000 rpm. Subsequently, 5.4 g of $FeCl_3 \cdot 6H_2O$ and 18.25 g of sodium oleate were added to the flask, and the mixture was heated at 70 °C for 4 hours. The flask was thereafter removed from the heat source, and the organic and aqueous phases were separated, with the organic phase being collected for further processing. The collected organic phase was washed thrice with MQ water to remove by-products and impurities, followed by solvent evaporation using a rota vapor until a viscous brown solution, serving as the precursor for IONPs was obtained.

2.2.2. Synthesis of IONPs

IONPs were synthesized following previous work. [10,22] In a 100 ml two-necked round bottom flask, 25 ml of ODE was added. OA and FeOl were defrosted and melted, following which 600 µL of OA and 1.6 g of FeOl were transferred into the flask. Stirring commenced at 300 rpm while heating gradually at the rate of 3 °C/min to the boiling point of ODE (318 °C) over 45 minutes, followed by cooling to 20 °C. Subsequently, 25 ml of hexane was added to the flask, and the mixture was transferred to a beaker containing 50 ml of isopropanol and 50 ml of acetone. IONPs were allowed to precipitate through a magnet for 10 minutes, after which the supernatant was discarded, and the precipitated particles were washed three times with acetone. Finally, the particles were redispersed in 30 ml of tetrahydrofuran (THF) and stored at 4 °C. The schematic workflow of IONPs synthesis by thermal decomposition of FeOl is depicted in Fig. 1(a).

To explore how different factors affect the properties of IONPs, we conducted a design of experiments (DOE). The Table 1 outlines the variables we studied and their ranges. For more details on how we set up

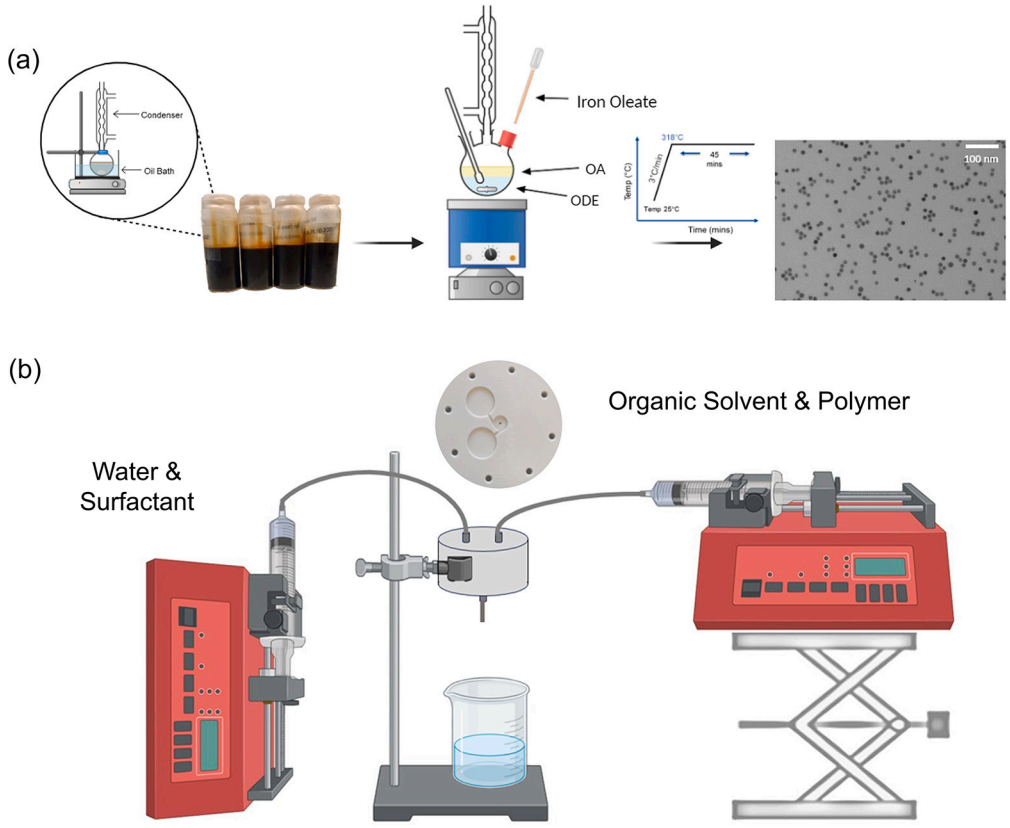

Fig. 1. (a) Schematic of thermal decomposition process for synthesis of IONPs, comprising a first step of synthesis of FeOl followed by controlled decomposition of the oleate at high temperature. (b) Schematic showing FNP for synthesis of bare PNPs and PLGA-coated IONPs.

Table 1
Variables and their ranges used in Design of Experiments (DOE) in connection to the synthesis of IONPs via thermal decomposition.

Variables	Range
OA amount (ml)	0.5-1.5
Ramp Rate (°C/min)	4-8
Dwell Time (min)	30-90
Solvent	BE, ES, ODE

Table 2
Variables studied and their ranges in FNP experiments for the synthesis of bare PNPs.

Variables	Range
Flow Rate of Aq. Phase (ml/min)	40 - 100
Polymer Wt.%	0.5 - 2
Surfactant Wt. %	0.1 - 1
Solvent	THF, Acetone, DMSO
Mode of Sample Collection	With/Without Quenching

our experiments, please refer to Table A.8 in the supplementary information.

2.2.3. Synthesis of bare polymeric nanoparticles (PNPs)

The synthesis of bare PNPs was carried out via FNP using a multi-inlet vortex mixer, having two inlets bringing fully miscible organic and aqueous phases (1 mm in diameter) into a central circular mixing part (6 mm in diameter). The design of the multi-inlet vortex mixer has been adapted from the initial work of Saad et al. [18] modified into a two-inlet mixer as has been reported in the work of Jezkova et al. [23] For reference, a schematic of FNP setup for the synthesis of bare PNPs and PLGA-encapsulated IONPs is shown in Fig. 1(b).

For a typical synthesis, PLGA was first dissolved in THF (1 wt.%) and loaded into a 20 ml sterile polypropylene syringe (luer slip connection to tubing), while an aqueous solution containing 0.1 wt.% Tween 80 (stabilizer) was loaded into a 120 ml polypropylene syringe (sterile catheter cone connection to tubing). The two solutions were injected into the mixer through two programmable syringe pumps (LAMBDA VIT-FIT (HP), LAMBDA Instruments GmbH); the flow rates were set to 100 ml/min for the aqueous stream and 10 ml/min for the organic stream. A transition time of 30 seconds was given to facilitate reaching a steady state, after which, samples were collected either directly from the mixer outlet (non-quenched) or diluted 10 times by volume in MQ water during collection (quenched).

To understand the influence of the operating and system variables in the FNP process on the size, size distribution and stability of the synthesized PNPs, the polymer wt.%, surfactant wt.%, solvent, flowrates of the aqueous and organic streams and mode of sample collection (quenching or no quenching) were varied as outlined in Table 2 above.

2.2.4. Functionalization of hydrophobic IONPs using FNP

Gaining insights from the influence of system and operating variables (in the FNP process) on physicochemical properties of bare PNPs as well as process operability, the FNP conditions for functionalization of the hydrophobic IONPs were chosen. The following were the set conditions: 1 wt.% of the polymer, 0.1 wt.% of Tween 80 (stabilizer), THF as organic solvent, 100 ml/min for aqueous phase, 10 ml/min for organic phase (THF). The final samples were collected without quenching. It must be noted that by functionalization, we mean phase transfer of IONPs combined with encapsulation of IONPs in PLGA. Such functionalized IONPs will be referred to as PLGA-encapsulated IONPs in this work. Further, worthy of note is that the polymer chosen for the functionalization studies was PLGA from BLD Pharmatech, unless stated otherwise.

Table 3
Overview of functionalized IONPs synthesized using FNP, showing the type and wt.% of IONPs used. Sample nomenclature PLGA_Solvent_L/H represents PLGA-encapsulated IONPs, IONPs being synthesized in solvent BE, ES or ODE and L (0.11) or H(0.34) representing wt.% of IONPs used during FNP.

Solvent used for IONP synthesis	Sample Label	Wt.% of IONPs
BE	PLGA_BE_L	0.11
BE	PLGA_BE_H	0.34
ES	PLGA_ES_L	0.11
ES	PLGA_ES_H	0.34
ODE	PLGA_ODE _L	0.11
ODE	PLGA_ODE _H	0.34

For the functionalization step, the FNP process was followed similarly to the synthesis of bare PNPs adding hydrophobic IONPs in the THF stream with final wt.% as mentioned in Table 3, leading to PLGA-encapsulated IONPs. These functionalized IONPs are named PLGA_solvent_L/H where the solvent refers to the solvent in which the hydrophobic IONPs were synthesized: BE, ES, and ODE; and L, H represent low and high weight % of IONPs in the THF stream as shown in Table 3. To separate the uncoated IONPs from the PLGA-encapsulated IONPs, a short magnetic separation (30s) was done and the bottom product, presumably containing the uncoated IONPs was discarded. The supernatant containing our desired phase transferred IONPs was further cleaned using four centrifugation cycles to remove the bare PNPs and surfactants, each at 8000 rpm for 5 minutes while decanting the supernatant by placing the centrifuged samples on the side of a magnet each time. The final bottom product containing primarily PLGA-encapsulated IONPs, was redispersed in 10 ml of MQ water and used for further characterization.

2.3. Characterization

To analyze the morphology and size of IONPs, a Tecnai 12 Transmission Electron Microscope (TEM) was used, while for bare PNPs and PLGA-encapsulated IONPs imaging and Energy Dispersive X-Ray spectra (EDS), Hitachi SU9000 Scanning (Transmission) Electron Microscope (S(T)EM) was used, after staining the samples with Phosphotungstic acid (PTA) (for further details refer to Appendix A.1).

Intensity-based H_d and ZP for both bare PNPs and PLGA-encapsulated IONPs were measured in a Litesizer 500, Anton Paar. Bare PNPs were taken as prepared while adequate dilutions for PLGA-encapsulated IONPs were made in MQ water prior to analysis. The crystallographic structure of IONPs was analyzed by X-ray diffraction (XRD) by using a Bruker D8 Advance da Vinci. IONPs were casted on the silica chip, dried, and covered with kapton film. The diffraction patterns were recorded with Cuka radiation (A = 1.5406 Å), with a scan ranging from 20° to 80° at a step size of 0.045°. The background signal in the XRD scan was removed by using DIFFRAC.EVA software while the peak analysis was done using PDF-5+. Saturation magnetization (Ms) of IONPs and PLGA-encapsulated IONPs were measured using a MicroMagTM 3900 Vibrating Sample Magnetometer (VSM) at 300 K. After VSM measurements, the gel capsules loaded with dried IONPs were digested in 69% Nitric Acid using Berghof SpeedWave XPERT prior to elemental analysis using an Agilent MP-AES 4210 Optical Emission Spectrometer to measure iron content (for further details refer to Appendix A.3).

2.4. Biocompatibility studies

2.4.1. Cell culture

Human dermal fibroblasts were isolated from human skin biopsy samples after taking the informed consent and cultured in DMEM (Dulbecco's Modified Eagle Medium) supplemented with 20% (v/v) FBS, 1% L-Glutamine, and 1% antibiotic-antimycotic solution.

2.4.2. Cytotoxicity assay

XTT assay was used to evaluate the in-vitro cytotoxicity of NPs in fibroblasts. The cells were seeded overnight in flat-bottomed 96-well plates at a density of 10,000 cells per well and then treated with increasing concentrations of bare PNPs and functionalized IONPs PLGA_BE_L/H, PLGA_ES L/H and PLGA_ODE_L/H i.e., 5, 10, 20, 40, 60, 80, and 100 μg/ml in triplicates for 24 hours. XTT solution was added to each well following manufacturer instructions and incubated at 37 °C in a CO_2 incubator for 4 hours. Later, the optical density of each well was measured through a Multiskan Sky Spectrophotometer (ThermoFisher Scientific, USA) at 450 nm wavelength.

Annexin-V and PI (Propidium Iodide) were used to evaluate the apoptotic effect of the bare PNPs and functionalized IONPs on human dermal fibroblasts. The cells were plated in six-well plates and treated with 100 μg/ml concentrations of bare PNPs, PLGA_BE_L, PLGA_ES_L and PLGA_ODE_L, separately and incubated for 24 hours. Afterward, the cells were trypsinized and washed with Annexin Binding Buffer (ABB). A 100 μL cocktail of Annexin-V and PI prepared in ABB was used for cell staining. After 20-30 minutes of incubation, the volume of the samples was made up to 300 μL with ABB, and analyses were performed by FACSDiva software using FACSAriaIII.

Analysis of nuclear morphology and area human dermal fibroblasts were grown on coverslips in six-well plates to detect nuclear morphology and measure the nuclear area to assess apoptosis induction. Cells were incubated for 24 hours in 100 μg/ml of each of the above NPs, separately. The cells were washed with phosphate-buffered saline (PBS) fixed with 4% paraformaldehyde and stained with 4,6-diamidino-2-phenylindole (DAPI) for 20 minutes. The cells were washed with PBS and imaged under a fluorescence microscope. The nuclear area of cells on each slide was calculated using ImageJ software.

3. Results and discussion

3.1. Synthesis of IONPs

To optimize the synthesis of IONPs in regards to their size, magnetic properties, and crystallinity within the thermal decomposition process of FeOl, we implemented a design of experiments (DOE) by incorporating four key input parameters: OA amount, concentration, temperature increase rate, dwell time, and the choice of solvent employed during the synthesis. The selected ranges for these input factors are mentioned in Table 1.

The incorporation of OA amount as a variable in our study is explained by its well-documented impact on the physico-chemical properties of IONPs. It has been mentioned in several reports that the nature, amount, and purity of OA that is added during the thermal decomposition reaction impacts the physico-chemical properties of IONPs. [24,25] Specifically, it is widely recognized that higher amounts of OA relative to FeOl result in the production of larger particles with narrower size distributions. [26]

Additionally, Demortiere et al. [27] have demonstrated that the addition of excess OA delays nucleation for several hours, enabling the manipulation of particle size through optimization of reaction time and OA amount. Hufschmid et al. [8] demonstrated that when the FeOl to OA ratio was 1:19, nucleation was delayed by approximately 2.5 hours. In our experimental design, in some of the syntheses, we are adding as much as twice the amount of OA in comparison to the standard method. Therefore, to counter the effect of delayed nucleation in a reaction mixture consisting of excess OA, dwell time is included as a second variable in our experimental design, with a range of 30-90 minutes.

The third input factor, ramp rate, governs the rate of temperature increase of the reaction mixture. Selecting an optimal ramp rate is crucial to produce monodisperse particles and avoid polydispersity resulting from overlapping nucleation and growth stages. For IONPs synthesis, an ideal ramp rate must strike a balance between being too rapid, lead-

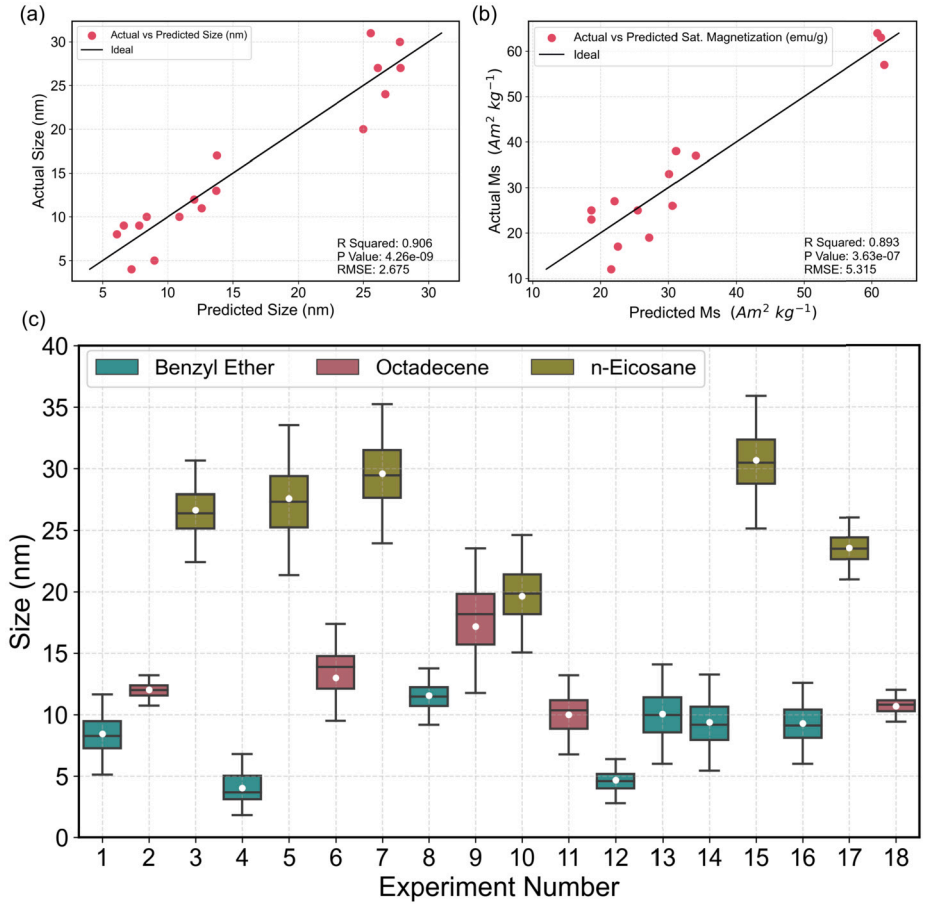

Fig. 2. (a) Comparison between measured and predicted particle sizes of IONPs. (b) Comparison between measured and predicted saturation magnetization values of IONPs, with experimental data fitted to standard least square models. (c) Boxplot illustrating the size distributions of IONPs synthesized under various experimental conditions detailed in Table A.8, categorized by solvent type: BE, ODE, and ES. The whiskers denote the range of IONP sizes, while the box represents the interquartile range. The median/second quartile is indicated by the black line within the box, and the mean sizes are denoted by white circles.

ing to polydisperse particles, and being too slow, significantly affecting particle size. [28]

The choice of reaction solvent is the fourth input factor for this study and it holds significant importance in thermal decomposition synthesis. Usually, ODE is used as a reaction solvent due to its impact on effective size control, but it may inadvertently diminish the magnetic properties of synthesized IONPs owing to the formation of non-magnetic phases along with the desired magnetite phase. [24] To address this concern, two alternative solvents, ES and BE, are selected. ES, characterized by a higher boiling point and longer chain length compared to ODE, is anticipated to exhibit greater stability against thermal degradation. Conversely, BE, known for its oxidizing effect during synthesis, is expected to favor the formation of oxidized phases of iron oxide (Fe_xO_y).

After performing experiments according to the experimental design, the output data were analyzed by fitting a linear regression model using the standard least squares method in JMP Statistical Software. This analysis revealed that, among the four input factors, the type of solvent used during IONPs synthesis influences both size and magnetic properties, from a statistical standpoint, supported by a low p-value of 0.00005. Conversely, the p-values for ramp rate, OA amount, and dwell time ranged from 0.38 to 0.50, suggesting a marginal statistical impact of these factors on the synthesis process. The prediction models show good fits for both the size and saturation magnetization (Ms) data of IONPs (Fig. 2a, b), further substantiated by root mean square error (RMSE) values of 2.675 for predicted size and 5.315 for Ms and regression coefficients of 0.90 for size and 0.89 for Ms. Based on these statistical findings, we chose to understand the role of reaction solvent in the thermal decomposition process through a judicious choice of characterization methods.

3.1.1. *Effect of reaction solvent on the size of IONPs*

Table 4 shows the influence of reaction conditions on the size of IONPs, assessed by analyzing representative TEM images using ImageJ software. Among the three solvents utilized for IONPs synthesis, BE yielded the smallest particles, while ODE and ES produced medium and larger-sized particles, respectively. Remarkably, this size trend remained consistent across the experimental design, regardless of other variables such as OA amount, ramp rate, or reaction duration.

Fig. 2(c) illustrates the size distribution of IONPs synthesized under varied conditions, with the x-axis indicating experiment number and the y-axis representing size in nanometers (nm), color-coded by solvent type. The blue boxes, representing BE solvent, consistently resulted in the smallest-sized particles across all experimental settings. Conversely, the green boxes, representing ES solvent, consistently produced the largest-sized particles regardless of other reaction parameters, while the red boxes, representing ODE solvent, fell between the sizes obtained with BE and ES solvents. This consistent trend underscores the significant influence of solvent choice on the size of synthesized IONPs, irrespective of other reaction parameters in complete concurrence with statistical model fitting.

To further validate the solvent's impact, three distinct syntheses were conducted by varying the solvent, while keeping all other reaction parameters constant. It can be seen from TEM images and size distribution of IONPs for these syntheses in Figs. 3(a, b, c) that results align very closely with our observations regarding solvent impact,

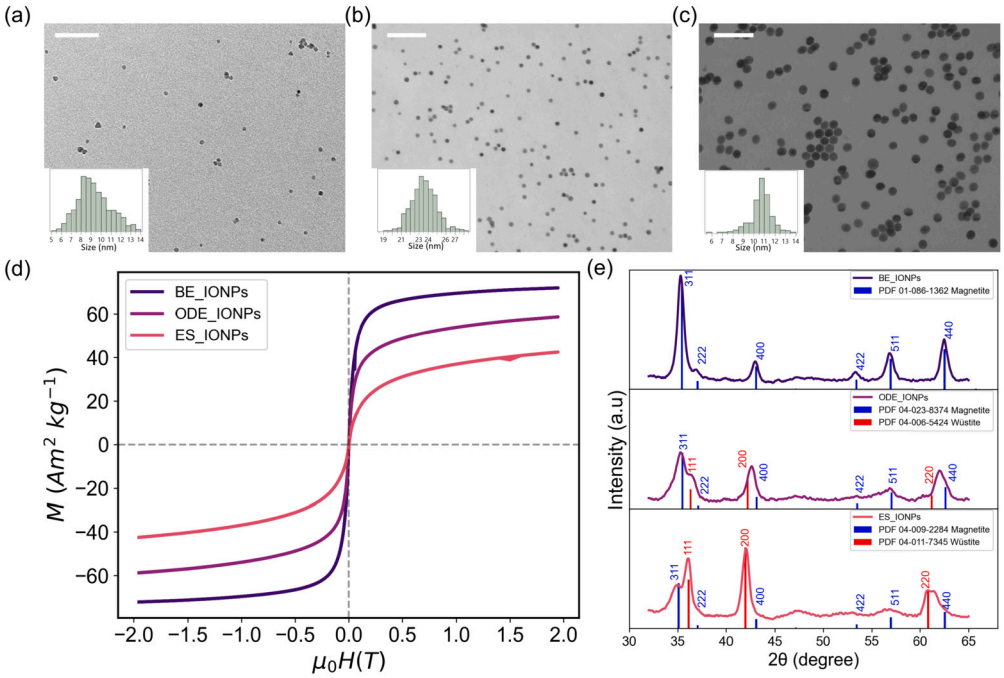

Fig. 3. (a-c) Representative TEM images of IONPs synthesized under identical conditions employing (a) BE, (b) ODE, and (c) ES, respectively. Insets depict size distributions calculated using ImageJ software. The scale bar in the TEM images represents 100 nm. (d) Magnetic hysteresis curves and (e) XRD spectra of IONPs synthesized at identical conditions utilizing various solvents.

Table 4
Overview of saturation magnetization (Ms) values, TEM sizes, and magnetic core sizes of IONPs synthesized in various reaction solvents. The input parameters for the synthesis of IONPs are detailed in the DOE column. For instance, 1.5_8_30 denotes the use of 1.5 mL of OA, a heating ramp rate of 8 °C/min, and a reflux time of 30 minutes. Values in brackets represent the normalized Ms after quantifying the organic content on IONPs surface through TGA.

Solvent	DOE	Ms (Am^2Kg^{-1})	TEM Size (nm)	Magnetic Core Size (nm)
ODE	1.5_8_30	38	12±1	12±3
	1.5_4_90	37	13±3	12±3
	0.3_4_30	34	17±4	13±3
	0.3_8_90	19	10±2	16±4
	0.9_6_60	26 (58)	11±1	14±3
ES	0.3_4_30	12	27±2	19±4
	1.5_8_30	17	28±3	17±3
	1.5_4_90	25	30±3	15±3
	0.3_8_90	25	20±3	15±3
	0.3_8_30	23	31±3	15±3
	0.9_6_60	27 (42)	24±1	14±3
BE	0.3_4_90	64	10±2	10±3
	1.5_8_90	57	9±2	11±3
	0.9_6_60	63 (75)	9±2	10±3

demonstrating a consistent trend where the mean size trend follows ES > ODE > BE.

The variation in nanoparticle size with changing reaction solvent is attributed primarily to differences in solvent boiling points. As suggested by Park, et al. [10] solvents with higher boiling points enhance the reactivity of FeOl, leading to the formation of larger particles. This hypothesis is supported by our findings, where ES (boiling point 340 °C) yielded the largest particles, while ODE (boiling point 318 °C) and BE (boiling point 290 °C) produced medium and the smallest-sized particles, respectively.

3.1.2. Effect of reaction solvent on magnetic properties

The magnetic properties of IONPs are known to depend on various factors, including the thickness of the organic coating, [29,30] phases of Fe_xO_y, [28] and the presence of a magnetically inert layer on the NPs surface. [31] In our study, it was observed that among all input factors, the choice of solvent during IONP synthesis exerted the most significant influence on magnetic properties. Notably, the magnetic saturation (Ms) was found to be highest when particles were synthesized in BE, whereas it was lowest when ES was employed as solvent.

The Ms values of IONPs synthesized in different solvents are summarized in Table 4. Specifically, when BE was used as the reaction solvent, the Ms reached as high as 64 Am^2Kg^{-1}, whereas in the cases of ODE and ES, the highest Ms values obtained were 38 Am^2Kg^{-1} and 27 Am^2Kg^{-1}, respectively. The comparatively lower Ms of IONPs in ODE and ES solvents can be attributed to three factors: (1) the presence of organic molecules like OA over the surface of IONPs, (2) the presence of a magnetically inert layer on the particle surface, and (3) reduced crystallinity. [32,33]

To validate these hypotheses, we initially characterized the particles through TGA. TGA analysis was employed to determine the organic content in three distinct IONPs samples, enabling the normalization of iron oxide content across the samples. Subsequently, after normalization, the Ms values of all three samples increased. However, the trend remained consistent, with particles synthesized in BE exhibiting the highest Ms, followed by those synthesized in ODE and ES, respectively as illustrated in Fig. 3(d).

After validating from the TGA results that the amount of organic content over IONPs' surface does not solely account for the diminished magnetic properties of ODE and ES synthesized IONPs, we calculated the magnetic core diameter of IONPs. This was achieved by fitting the Langevin function over the hysteresis loop (for more information refer to Fig. A.7) and comparing the magnetic core size with the physical size of IONPs determined from representative TEM images (refer to Table 4). The magnetic core size of IONPs synthesized in BE closely matched their physical size. Conversely, the largest disparity between physical and magnetic sizes was observed in IONPs synthesized in ES. This significant difference indicates that a substantial portion of ES-synthesized

IONPs may not contribute to the magnetic properties. This effect can be ascribed to the presence of a small fraction of antiferromagnetic phase (e.g. hematite or wüstite). [34]

To determine the phases of Fe_xO_y in the samples, we utilized the powder XRD technique. The XRD patterns of IONPs synthesized in BE, ES, and ODE are presented in Fig. 3(e). In spectra corresponding to IONPs synthesized in BE, well-defined reflection associated with the inverse spinal structure of Fe_xO_y is evident, including (311), (222), (400), (422), (511), and (440). These reflections exhibit superior crystallinity compared to those synthesized in ES and ODE, aligning closely with reference peaks of magnetite, indicative of magnetic spinal phases of Fe_xO_y. While the peaks in the spectra of ES and ODE overlap with reference peaks of both magnetite and wüstite phases of Fe_xO_y indicating a presence of antiferromagnetic phase along with spinal phases of Fe_xO_y in synthesized IONPs.

One proposed explanation for the difference in magnetic properties of IONPs, when a solvent is varied, involves the deviation of the reaction pathway toward nonspecific reactions at elevated temperatures during thermal decomposition, resulting in the production of various byproducts including H_2, CO, CO_2, alkenes, and ketones. These nonspecific reactions diminish the selectivity of the thermal decomposition pathway, leading to an increased occurrence of strain-inducing defects. [35] Additionally, radical species generated at high temperatures contribute to driving the reaction pathway toward the formation of a less oxidized and antiferromagnetic phase of Fe_xO_y (wüstite or hematite phase) by depleting the available oxygen in the system. [36,37] In contrast to ODE and ES, particles synthesized in BE exhibited heightened magnetism, possibly due to the synthesis occurring at relatively lower temperatures (due to its lower boiling point compared to ODE and ES), reducing radical species formation and enhancing the specificity of thermal decomposition. Moreover, upon thermolysis, BE acts as an oxidizing agent, directing the reaction pathway toward the synthesis of oxidized and highly magnetic phases. [11]

3.2. Flash nanoprecipitation

The synthesized IONPs, owing to organic coating (OA) are non-dispersible in water, which, however, is necessary for their applicability in biomedicine. Therefore, we have focused on a robust and scalable FNP process to enable phase transfer (organic to aqueous) of the IONPs and provide polymer functionalization of the IONPs. To select the optimum conditions for phase transfer, we studied the effect of operation and system variables on the size, size distribution, and stability of PLGA PNPs. Following this, the effects of IONPs amount and hydrophobicity were studied on the physico-chemical properties of the functionalized IONPs.

3.2.1. Synthesis of bare PNPs

FNP was used to synthesize bare PNPs of PLGA by rapidly micromixing two miscible streams in a multi-inlet vortex mixer - one containing molecularly dissolved PLGA in THF (1 wt.%) at 10 ml/min and the other containing stabilizer Tween 80 dissolved in water (0.1 wt.%) at 100 ml/min. When both the streams are turbulently mixed inside the reactor, PLGA being hydrophobic, exceeds its solubility limit, causing local supersaturation that leads to spontaneous nucleation of PLGA particles. Such nuclei continuously grow by addition of polymer chains consuming the supersaturation in the system, while some aggregation events also happen among the growing particles, however, those being stabilized by the presence of Tween 80. The obtained PNPs collected by quenching the mixture at the outlet, show a H_d of 114 ± 1 nm, and a zeta potential of -31 ± 1 mV. Here, the standard deviations originate from triplicate measurements of two different independent experiments under the same conditions. Fig. 4(a) shows a representative TEM image of the same PNPs with an inset of the histogram showing particle size distribution calculated using ImageJ software. The PLGA NPs appear brighter against the dark PTA stain as confirmed by the EDS line scan cutting through the particle of interest (Fig. 4(b)). The size obtained from TEM is 69 ± 13 nm, which is smaller than the H_d. While DLS measures H_d based on scattering due to the Brownian motion of suspended particles in solution, TEM measures the dry radius based on the electrons transmitted through a thin slice of the sample. The H_d assumes that the particles are spherical in shape, accounts for ligands bound to the surface of the particles and weak interparticle dipolar interactions among NPs causing weak interparticle coupling as reported previously. [38]

3.2.2. Influence of FNP conditions on bare PNPs

With an aim to decide on the operation and system variables to be used in the FNP process for the phase transfer of IONPs, we varied surfactant wt.%, flowrates of the aqueous and organic streams, polymer wt.%, mode of sample collection (quenching or no quenching) and solvent, as outlined in Table 2. The influence of these variables on the size, size distribution, and colloidal stability of the bare PNPs was investigated.

Fig. 4(c) shows H_d of such PLGA PNPs, synthesized using 0.5 and 2 wt.% of PLGA, the flowrate of the organic stream being 10 ml/min, the aqueous stream being 100 ml/min with a surfactant concentration of 0.1 wt.%. The error bars indicate standard deviations of triplicate measurements for each independent experiment performed under the same conditions and represented by a single bar in the figure. Our measurements show high repeatability of the FNP experiments with standard deviations of the size distributions ranging between 3 - 6 nm for the lower and higher wt.% of the polymers respectively.

Increasing surfactant wt.% has no significant effect on the H_d of the PNPs at both low and high polymer wt.% (Fig. A.8). It may be noted that the surfactant concentration is well above the critical micelle concentration of Tween 80 (0.0016 wt.%) for all FNP experiments.

Fig. 4(d) shows that an increased aqueous flow rate leads to a decrease in the PNPs size for a higher polymer wt.%, while there is no significant influence at the lower polymer wt.%. An increasing aqueous flow rate leads to a decreasing organic solvent fraction and hence higher supersaturation, defined as the ratio of the concentration of the polymer to the equilibrium concentration in the mixed solvent system. This further leads to an enhanced nucleation rate or a higher number of nucleation events resulting in smaller particles. [39]

Fig. 4(e) shows the H_d of PNPs obtained by varying the wt.% of the polymer in the organic stream. As the wt.% of the polymer increases, the H_d of the PNPs increases. In this anti-solvent precipitation process, an increase in wt.% of the precipitating component (polymer) will increase the supersaturation. A higher supersaturation is expected to enhance the nucleation rate, leading to smaller particle sizes. However, an increased wt.% also leads to the confinement of a large number of polymer chains in a reduced volume, favoring aggregation-dominated growth of the formed PNPs, thereby leading to an increase in size.

It may be noted that these samples are collected by quenching the reaction volume at the mixer outlet, whereby diluting the suspension ten times by volume. When the samples are collected without quenching, all the H_d measured are slightly higher (Fig. A.9). These smaller sizes may be explained by the prevention of further aggregation among formed PNPs or the measurement of more dilute suspensions (in the latter case) using dynamic light scattering, leading to reduced interparticle interactions, or a combination of both effects. However, without quenching, the processability of the PNPs, such as solvent removal, freeze-drying, etc. is less energy consuming, and therefore, we chose to not quench our samples at the mixer outlet.

The effect of solvent type on the H_d of bare PNPs is reported in Fig. 4(f). For all three solvents studied, increased polymer wt.% results in larger H_d as explained above. Interestingly, the bare PNPs synthesized in the presence of acetone show the smallest H_d, followed by those in DMSO and finally in THF. Supersaturation levels can be impacted by changing PLGA concentration or its solubility in the mixed solvent, both of which will be affected by the nature of the solvent. Higher solubility

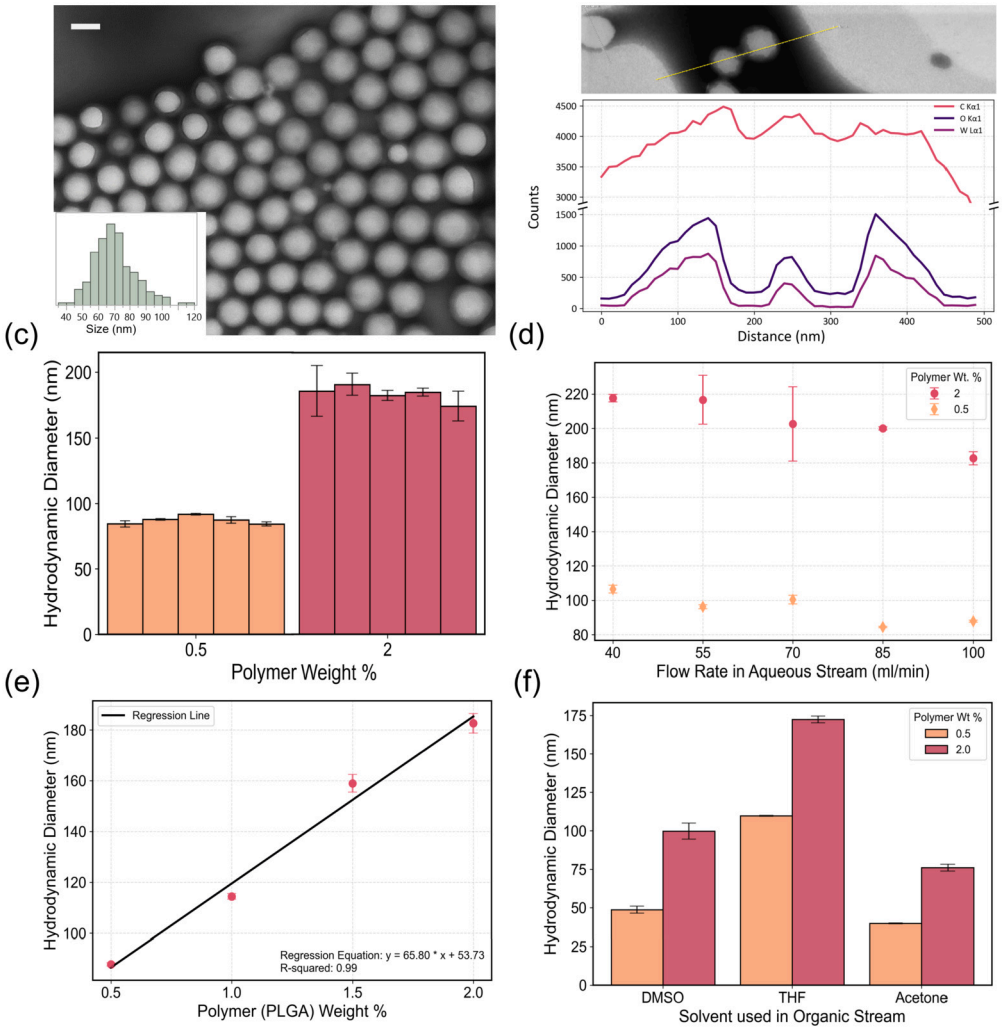

Fig. 4. (a) Representative TEM image of bare PNPs with inset histogram showing size distribution measured using ImageJ software and scale bar of the image is 100 nm (b) EDS spectra of bare PNPs. (c) H_d of bare PNPs synthesized using two different polymer wt.% showing high repeatability of the FNP process. (d) Effect of aqueous stream flow rate on the size of bare PNPs. (e) Effect of increasing polymer wt.% on H_d of bare PNPs. (f) Effect of different solvents (used in the FNP process) on size of bare PNPs. These final experiments have been conducted with PLGA from BLD Pharmatech, which is the representative polymer used for the phase transfer of IONPs.

of PLGA in acetone combined with high miscibility of acetone in water leads to high supersaturation in the mixed solvent, resulting in smaller particles. [40]

Although the size and colloidal stability of the bare PNPs is an important consideration for choosing the optimum conditions to perform the FNP for the functionalization of IONPs, it must be noted that these design conditions may be affected by the physicochemical properties of the IONPs. In our case, the IONPs precipitate in acetone but are dispersible in THF. THF with a low boiling point of 65 °C, enables easy removal of the solvent either by vacuum operation or dialysis, [18] while DMSO has a higher boiling point of 189 °C and can only be removed by dialysis, complicating post-processing of the PNPs. Thus, we chose THF as the solvent in our studies. As the surfactant concentration did not have any significant influence on the PNPs properties, we chose 0.1 wt.%, the lowest weight percent studied herein, albeit, the concentration was higher than critical micelle concentration of the surfactant. While the lowest polymer wt.% produced PNPs with the smallest size (≈ 100 nm), we chose 1 wt.% to ensure a high enough yield of NPs during the synthesis process. Consequently, the aqueous flow rate was set to 100 ml/min since, a higher flow rate leads to smaller PNPs, especially for higher polymer wt.%.

3.3. Functionalization of IONPs using FNP

To facilitate phase transfer of the hydrophobic IONPs, we modified the FNP process explained above by dispersing the IONPs synthesized via thermal decomposition in the THF stream, along with 1 wt.% PLGA. The THF stream was allowed to mix in the multi-inlet vortex mixer against an opposing stream of water containing 0.1 wt.% Tween 80. After the collection of sample, a short magnetic separation was done and the bottom product, presumably containing the uncoated IONPs was discarded. The supernatant containing our desired functionalized IONPs was further cleaned using centrifugation and magnetic decantation to remove bare PNPs. Fig. 5(a) shows a representative TEM image of functionalized IONPs using IONPs synthesized in ODE, with an inset histogram showing the particle sizes measured using ImageJ software. The brighter particles against a dark background of PTA stain represent PLGA spheres, similar to the bare PNPs, while the darker particles represent IONPs. To confirm the presence of IONPs inside the PLGA spheres, an EDS analysis was carried out across several line scans cutting through such particles. Representative spectra shown in Fig. 5(b), show that the tungsten (W) signal drops as soon as the beam hits the brighter PLGA sphere and picks up after reaching the edge of the sphere. Further, as the beam strikes each IONPs inside the PLGA sphere, a bump in the iron (Fe) as well as oxygen (O) spectra is distinctively noticed. The function-

Table 5
TEM and H_d sizes of functionalized IONPs synthesized at two different wt.% of IONPs. The IONPs were synthesized in three different solvents namely, BE, ES, and ODE. Sample names of the functionalized IONPs are labeled as PLGA_solvent_L/H where L and H denote low and high wt.% of IONPs. Wt.% of the IONPs used for FNP is calculated based on MP-AES digestion of the IONPs. Error bars for TEM indicate standard deviations of particle size distributions measured using ImageJ, whereas error bars for DLS measurements are standard deviations from triplicate measurements.

Sample labels	Theoretical Wt.% of IONPs	Wt.% of IONPs calculated from MP-AES	TEM size (nm)	H_d size (nm)
PLGA_BE_L	0.11	0.07	86 ± 23	223 ± 4
PLGA_BE_H	0.34	0.22	94 ± 19	265 ± 5
PLGA_ES_L	0.11	0.08	73 ± 15	237 ± 4
PLGA_ES_H	0.34	0.25	79 ± 15	250 ± 4
PLGA_ODE_L	0.11	0.01	69 ± 22	236 ± 1
PLGA_ODE_H	0.34	0.03	183 ± 49	242 ± 8

alized IONPs are readily dispersible in water, unlike the IONPs, and also show a zeta potential (ZP) of -29 ± 1 mV, which is hypothesized to originate from the hydrolysis of surface ester end group PLGA [41]. Nuclear magnetic resonance [47,48] was performed to confirm the presence of ester end groups on the PLGA used (Fig. A.13) As can be seen from Fig. 5(a), the loading of PLGA spheres with IONPs is not uniform. To further optimize this, we chose two different sizes of hydrophobic IONPs viz. 7 ± 1 nm, 14 ± 2 nm, synthesized in different solvents i.e. BE and ES respectively (for further information refer to A.10) and varied their wt.% in the organic stream. Fig. A.13 shows the H_d of the functionalized IONPs in comparison to the bare PNPs, synthesized under otherwise identical conditions. The H_d of all the functionalized IONPs are higher than the bare PNPs, indicating possible encapsulation of IONPs within the PLGA spheres. Previous reports have shown that control of NPs size in FNP process employing hydrophobic core material and amphiphilic polymer, such as a block co-polymer, is accomplished through two process variables: the percent core of the formulation and the total mass concentration of solids in the solvent stream. [42] The total mass concentrations of solids in the solvent stream increase from 9.6 mg/ml to 11 mg/ml for PLGA_BE and from 9.8 mg/ml to 10.7 mg/ml for PLGA_ES for low and high wt.% respectively, while the corresponding percent cores change from 7.7 to 19.9 and 9.7 to 17.8 respectively, leading to an increase in H_d as shown in Fig. A.13. Compared to the bare PNPs, all the functionalized IONPs show higher colloidal stability with ZP < -30 mV. The negative surface charge on the functionalized IONPs, originating from the functional groups of PLGA, further confirms the successful encapsulation of IONPs within the PLGA spheres. The combined effects of electrostatic and steric stabilization are likely responsible for the overall colloidal stability of the PLGA-encapsulated IONPs.

Figs. 5(c)-(f) show representative TEM images of phase transferred IONPs for two different wt.% i.e. 0.11 and 0.34 in the organic solvent (see Table 5). The sizes of the PLGA-encapsulated IONPs for the different samples range from 86 ± 23 nm, 94 ± 19 nm (PLGA_BE_L and PLGA_BE_H respectively) and 73 ± 15 nm, 79 ± 15 nm (PLGA_ES_L and PLGA_ES_H, respectively). At lower wt.% of IONPs, it is evident from Fig. 5(c) that the PLGA spheres (in the case of PLGA_BE_L) are heavily loaded with IONPs and bare PNPs are not directly observed. A similar observation is also noted in Fig. 5(d) for higher wt.% of IONPs ((PLGA _BE_H). On the other hand, for PLGA_ES_L (Fig. 5(e)), i.e. when low wt.% of IONPs is used in the FNP process, one can note the appearance of low loadings of IONPs in the PLGA spheres and also bare PNPs. The PLGA spheres became saturated with IONPs (sample PLGA_ES_H, Fig. 5(f)) similar to the case of PLGA_BE_H when the wt.% of IONPs was increased theoretically from 0.11 to 0.34. Digestion of these PLGA-encapsulated IONPs, followed by analysis of elemental Fe content in the samples reveals that encapsulation efficiency of IONPs increases from 30.3% to 43.4% for PLGA_BE_L and PLGA_BE_H respectively, whereas this increases significantly from 7.6% to 36.4% for PLGA_ES_L and PLGA_ES_H, respectively. The significant increase in the latter case concurs well with the visual impressions from the TEM images of PLGA_ES_L and PLGA_ES_H and suggests that a higher number of IONPs are packed per PLGA sphere for PLGA_ES_H, with no apparent increase in the final size. Although the focus of our work has not been to elucidate the mechanism of IONP encapsulation, it may be hypothesized that the differences in loading efficiencies may arise primarily from the size of the IONPs - a smaller size, leading to higher loading efficiencies, owing to higher initial particle numbers of IONPs added to the organic solvent prior to FNP. Varying the size of the hydrophobic IONPs interrogates the effect of diffusion and assembly time scales in FNP, whereby for producing a single population of PLGA-encapsulated IONPs, diffusion time scales of the amphiphilic polymer (PLGA) globule and hydrophobic IONPs must match.

Table 6
Overview of measured wt.% and calculated particle numbers of IONPs used for various encapsulation reactions in FNP. Measured PLGA wt.% and IONPs encapsulation efficiencies are reported for all functionalized IONPs, prepared in three different solvents at lower and higher wt.% of IONPs.

Sample	wt.% of IONPs	No. of IONPs	PLGA wt.%	Encapsuation Efficiency of IONPs
PLGA_BE_L	0.07	1.1E+16	68	30.3
PLGA_BE_H	0.25	2.4E+16	60	43
PLGA_ES_L	0.07	1.2E+15	90	7.6
PLGA_ES_H	0.22	2.6E+15	68	36.4
PLGA_ODE_L	0.01	1.0E+16	48	8.1
PLGA_ODE_H	0.03	3.0E+16	44	9.6

To further understand the effect of size, we chose a third IONPs, synthesized in ODE, having a size of 7 ± 1 nm (similar to the IONPs synthesized in BE, for further information refer to - A.10). When FNP was carried out at the lower wt.%, with these IONPs, the TEM sizes of the phase transferred IONPs were obtained to be 69 ± 22 nm, similar to those of PLGA_BE_L. However, it is noteworthy from the representative TEM image of PLGA_ODE_L (Fig. 5(g)), that the distribution of IONPs per PLGA sphere is lower and non-uniform in comparison to PLGA_BE_L (Fig. 5(c)), further supported by a lower encapsulation efficiency of IONPs i.e. 8.1% which is similar to PLGA_ES_L. However, an increase in the wt.% of IONPs, leads to increased sizes (183 ± 49 nm), with no significant increase in encapsulation efficiency (9.6%). These observations do not completely agree with the influence of IONPs size as the only variable on the final particle size of the functionalized IONPs and the resultant encapsulation efficiencies. MP-AES digestion of the IONPs followed by determination of elemental Fe shows that the IONPs synthesized in ODE have a higher organic content than those in BE by 66%, (refer to Table 6). If one calculates the number of particles added (for the same mass of IONPs) in the FNP process, it can be seen from Table 6, that there is no significant difference between the number of IONPs added in case of PLGA_BE and PLGA_ODE. Therefore, it may be hypothesized that the differences in the resultant properties of PLGA_ODE emanate from the hydrophobicity differences between the IONPs used for FNP.

To our knowledge, such reports are not abundant in the literature when it comes to colloidal IONPs encapsulation using FNP. In the case of the PLGA_ODE, we hypothesize that the ODE IONPs have a faster anti-solvent precipitation tendency in comparison to BE IONPs, while the rate of anti-solvent precipitation of PLGA (1 wt.%) remains same. In this process, the IONPs will aggregate due to hydrophobic forces, before they meet the polymer chains, leading to higher sizes of PLGA_ODE_L in comparison to PLGA_BE_L. This hydrophobic interaction will further be enhanced due to increasing wt.% in the case of PLGA_ODE_H leading to higher sizes with higher loadings of IONPs. However, our calculated en-

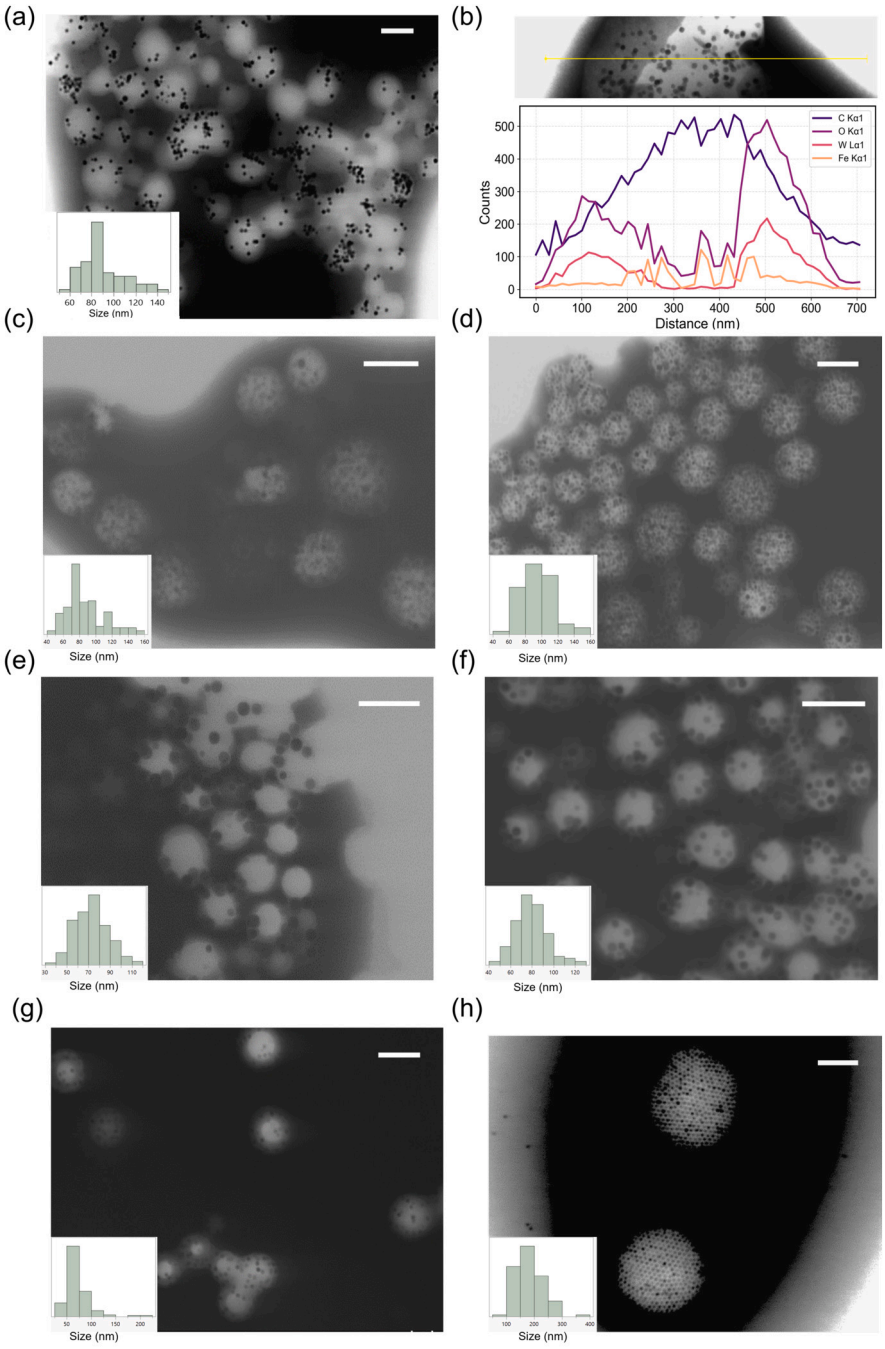

Fig. 5. (a) Representative S(T)EM image of PLGA-encapsulated IONPs with inset showing size distribution measured using ImageJ software. (b) EDS Spectra of PLGA-encapsulated IONPs (PLGA with known groups was used for a and b). Representative S(T)EM images of (c) PLGA_BE_L, (d) PLGA_BE_H, (e) PLGA_ES_L, (f) PLGA_ES_H, (g) PLGA_ODE_L and (h) PLGA_ODE_H respectively with insets showing size distributions measured using ImageJ software. Scale bar of the S(T)EM images is 100 nm.

capsulation efficiencies in this case do not vary significantly than in the case of PLGA_ODE_L, since, representative TEM images show that the increase in size is directly proportional to the IONPs loading per PLGA sphere. It may be noted that all functionalized IONPs do not show a significant change in the nature of the magnetization curves in comparison to the bare IONPs (Fig. A.11). Although a detailed understanding of the mechanism leading to PLGA-encapsulated IONPs is beyond the scope of this work, our preliminary findings indicate that size as well as hydrophobicity of the IONPs combinedly controls this. In essence, the supersaturations of the components PLGA and IONPs, influence their precipitation tendencies while their diffusion time scales control successful encapsulation.

3.4. Biocompatibility studies

Cell viability assay is one of the most common methods to assess the biocompatibility of NPs. The proliferation rate is an essential indicator for determining the health of cells and the potential of NPs to affect growth processes. [43] Here, we examined the viability of human dermal fibroblasts treated with various concentrations (5-100 μg/ml) of NPs namely Bare PNPs, PLGA_BE_L/H, PLGA_ES_L/H and PLGA_ODE_L/H, through XTT assay. Results showed no effect of the NPs on cell viability after 24 hours (Fig. 6(a)). The biocompatibility of the PLGA-encapsulated IONPs (PLGA_BE_L, PLGA_ES_L and PLGA_ODE_L and Bare PNPs) at 100 μg/mL concentrations was confirmed by the apoptosis assay using Annexin-V and PI staining. The results showed that all

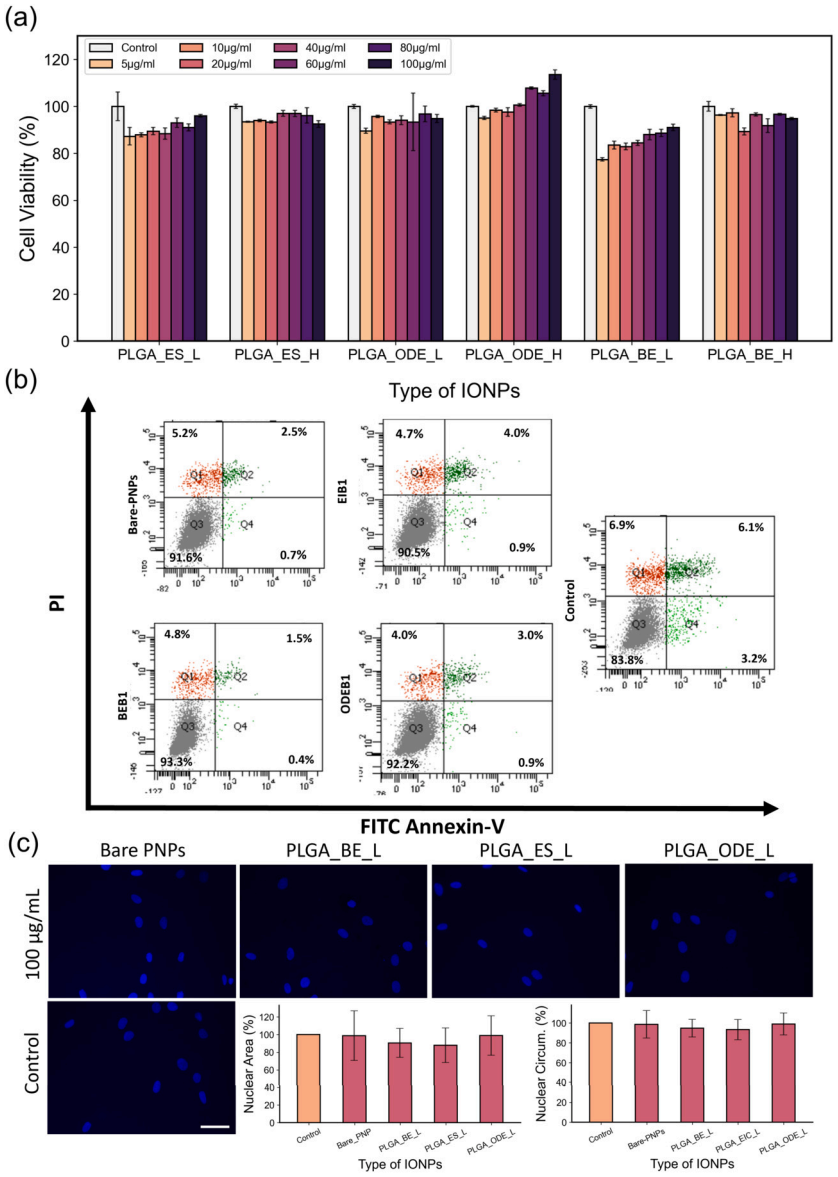

Fig. 6. (a) Cell viability assays of NPs namely bare PNPs, PLGA BE_L/H, PLGA ES_L/H, and PLGA ODE_L/H at different concentrations (5-100 µg/ml) performed in human dermal fibroblasts. (b) Apoptosis assays of selected NPs and corresponding (c) Fluorescence images of DAPI stained nuclei and calculated nuclear areas for selected NPs.

PLGA-encapsulated IONPs and bare PNPs showed < 10% apoptotic and necrotic cells, similar to the control group. In this study, DAPI analysis was performed to assess nuclear morphology and measure the nuclear size to detect the changes in the nuclei of cells due to the apoptotic effect. DAPI provides specificity and quantifiable analyses of nuclear content. [44,45] The fluorescence images of DAPI-stained nuclei showed normal morphology and no nuclear blebbing (a characteristic feature of apoptosis) in nuclei of IONPs' treated fibroblasts, which were similar to untreated cells' nuclei. The quantification data showed that the nuclear area and circumference of the nuclei were identical to the control group. A previous study also reported the biocompatible behavior of functionalized IONPs on human follicle dermal papilla cells. [46] These outcomes indicate that these functionalized IONPs can be used effectively in various biomedical applications since they did not show any cytotoxic effect on healthy cells.

4. Conclusion

With an aim to understand the effect of various reaction conditions such as the amount of ligand, ramp rate, dwell time, and solvent, in the thermal decomposition of FeOl to produce IONPs, we performed a detailed design of experiments. Our study highlighted the significance of solvent type on the size, magnetic properties, and crystallinity of the IONPs. By varying the solvent type, IONPs with a tunable size range (10-30 nm) having magnetic properties (75 to 42 Am^2Kg^{-1}) were synthesized. Three representative IONPs of different sizes were phase-transferred and functionalized using FNP to yield polymer-coated IONPs, a process being reported here for the first time. Previous reports in the literature [42] have focused on encapsulation of organic molecules such as drugs or collapsed polymers, whereby size control of resultant PNPs is shown to be influenced by the percent core of the formulation and the total mass concentration of solids in the solvent stream. Our novel approach, focusing on encapsulation of inorganic colloids (larger than the above reported molecules), shows that the resultant particle sizes and IONPs loading efficiencies may be controlled not only by the sizes of the IONPs but also by their hydrophobicities, (measured through their organic contents) Our findings lay the foundation for exploring the influence of the physico-chemical properties of IONPs on the eventual encapsulation of IONPs in PLGA spheres. The PLGA-encapsulated IONPs were observed to have high colloidal stabil-

ity and showed no discernible cytotoxicity in human dermal fibroblasts, thereby paving the way for their applications within biomedicine. However, future investigations should focus on deepening our understanding of the encapsulation mechanism and the interactions between IONP features and the PLGA matrix. Unraveling these features, will enable precise control over particle loading, aligning with the specific needs of various biomedical applications.

CRediT authorship contribution statement

Sulalit Bandyopadhyay: Writing – review & editing, Writing – original draft, Supervision, Project administration, Formal analysis, Data curation. **Haroon Zafar:** Writing – review & editing, Writing – original draft, Visualization, Investigation, Formal analysis, Data curation. **Muhammad Sarmad Khan:** Writing – review & editing, Investigation, Data curation. **Reema Ansar:** Writing – review & editing, Investigation, Data curation. **Davide Peddis:** Writing – review & editing, Investigation. **Sawssen Slimani:** Writing – review & editing, Investigation. **Nesrine Bali:** Writing – review & editing. **Zahra Sajid:** Writing – original draft, Investigation. **Rida e Maria Qazi:** Writing – original draft, Investigation. **Fawad ur Rehman:** Writing – original draft, Investigation. **Afsar Ali Mian:** Writing – original draft, Investigation.

Declaration of competing interest

The authors declare that they have no known competing financial interests or personal relationships that could have appeared to influence the work reported in this paper.

Data availability

No data was used for the research described in the article.

Acknowledgement

We acknowledge the Research Council of Norway for their support of the Norwegian Micro - and Nano-Fabrication Facility, NorFab, under project number 295864. This work is supported by the funding of Wellcome Leap (project 53452). The DLS and zeta potential measurements were conducted at the Particle Engineering Core Facility, Norwegian University of Science and Technology (NTNU). We extend our gratitude to Vyshnav Punnath Sivasankaran, PhD Candidate at the Particle Engineering Centre, for synthesizing several batches of IONPs. Additionally, we appreciate the assistance of the AKU-CRM Core Facility staff, particularly Mr. Areeb Ahmed, for conducting the flow cytometry experiments.

Appendix A. Supplementary material

Supplementary material related to this article can be found online at https://doi.org/10.1016/j.jcis.2024.09.134.

References

[1] S. Khizar, A.A. Al-Dossary, N. Zine, N. Jaffrezic-Renault, A. Errachid, A. Elaissari, Contribution of magnetic particles in molecular diagnosis of human viruses, Talanta 241 (2022) 123243.
[2] N. Ahmed, N.M. Ahmad, H. Fessi, A. Elaissari, In vitro mri of biodegradable hybrid (iron oxide/polycaprolactone) magnetic nanoparticles prepared via modified double emulsion evaporation mechanism, Colloids Surf. B, Biointerfaces 130 (2015) 264–271.
[3] Y. Cui, M. Zhang, F. Zeng, H. Jin, Q. Xu, Y. Huang, Dual-targeting magnetic plga nanoparticles for codelivery of paclitaxel and curcumin for brain tumor therapy, ACS Appl. Mater. Interfaces 8 (47) (2016) 32159–32169.
[4] H. Etemadi, J.K. Buchanan, N.G. Kandile, P.G. Plieger, Iron oxide nanoparticles: physicochemical characteristics and historical developments to commercialization for potential technological applications, ACS Biomater. Sci. Eng. 7 (12) (2021) 5432–5450.
[5] S. Khizar, E. Elkalla, N. Zine, N. Jaffrezic-Renault, A. Errachid, A. Elaissari, Magnetic nanoparticles: multifunctional tool for cancer therapy, Expert Opin. Drug Deliv. 20 (2) (2023) 189–204.
[6] S.M. Dadfar, K. Roemhild, N.I. Drude, S. von Stillfried, R. Knüchel, F. Kiessling, T. Lammers, Iron oxide nanoparticles: diagnostic, therapeutic and theranostic applications, Adv. Drug Deliv. Rev. 138 (2019) 302–325.
[7] S. Famiani, A.P. LaGrow, M.O. Besenhard, S. Maenosono, N.T.K. Thanh, Synthesis of fine-tuning highly magnetic fe@ fe x o y nanoparticles through continuous injection and a study of magnetic hyperthermia, Chem. Mater. 30 (24) (2018) 8897–8904.
[8] R. Hufschmid, H. Arami, R.M. Ferguson, M. Gonzales, E. Teeman, L.N. Brush, N.D. Browning, K.M. Krishnan, Synthesis of phase-pure and monodisperse iron oxide nanoparticles by thermal decomposition, Nanoscale 7 (25) (2015) 11142–11154.
[9] S. Laurent, D. Forge, M. Port, A. Roch, C. Robic, L. Vander Elst, R.N. Muller, Magnetic iron oxide nanoparticles: synthesis, stabilization, vectorization, physicochemical characterizations, and biological applications, Chem. Rev. 108 (6) (2008) 2064–2110.
[10] J. Park, K. An, Y. Hwang, J.-G. Park, H.-J. Noh, J.-Y. Kim, J.-H. Park, N.-M. Hwang, T. Hyeon, Ultra-large-scale syntheses of monodisperse nanocrystals, Nat. Mater. 3 (12) (2004) 891–895.
[11] R. Chen, M.G. Christiansen, A. Sourakov, A. Mohr, Y. Matsumoto, S. Okada, A. Jasanoff, P. Anikeeva, High-performance ferrite nanoparticles through nonaqueous redox phase tuning, Nano Lett. 16 (2) (2016) 1345–1351.
[12] E.C. Vreeland, Development of Novel Synthetic Methods for Size-Tunable Synthesis of Superparamagnetic Iron Oxide Nanoparticles, The University of New, Mexico, 2014.
[13] F. Herranz, M.P. Morales, A.G. Roca, M. Desco, J. Ruiz-Cabello, A new method for the rapid synthesis of water stable superparamagnetic nanoparticles, Chemistry 14 (30) (2008) 9126–9130.
[14] M. Wang, M.-L. Peng, W. Cheng, Y.-L. Cui, C. Chen, A novel approach for transferring oleic acid capped iron oxide nanoparticles to water phase, J. Nanosci. Nanotechnol. 11 (4) (2011) 3688–3691.
[15] J. Xie, C. Xu, N. Kohler, Y. Hou, S. Sun, Controlled pegylation of monodisperse fe3o4 nanoparticles for reduced non-specific uptake by macrophage cells, Adv. Mater. 19 (20) (2007) 3163–3166.
[16] Z. Hou, Y. Liu, J. Xu, J. Zhu, Surface engineering of magnetic iron oxide nanoparticles by polymer grafting: synthesis progress and biomedical applications, Nanoscale 12 (28) (2020) 14957–14975.
[17] H. Nosrati, M. Salehiabar, S. Davaran, A. Ramazani, H.K. Manjili, H. Danafar, New advances strategies for surface functionalization of iron oxide magnetic nano particles (ionps), Res. Chem. Intermed. 43 (2017) 7423–7442.
[18] W.S. Saad, R.K. Prud'homme, Principles of nanoparticle formation by flash nanoprecipitation, Nano Today 11 (2) (2016) 212–227.
[19] B. Sulalit, E. Mani, Design and modeling of sub-micron particles via precipitation, 2023.
[20] J. Tao, S.F. Chow, Y. Zheng, Application of flash nanoprecipitation to fabricate poorly water-soluble drug nanoparticles, Acta Pharm. Sin. B 9 (1) (2019) 4–18.
[21] Y. Liu, G. Yang, D. Zou, Y. Hui, K. Nigam, A.P. Middelberg, C.-X. Zhao, Formulation of nanoparticles using mixing-induced nanoprecipitation for drug delivery, Ind. Eng. Chem. Res. 59 (9) (2019) 4134–4149.
[22] A. Sharma, J.W. Foppen, A. Banerjee, S. Sawssen, N. Bachhar, D. Peddis, S. Bandyopadhyay, Magnetic nanoparticles to unique dna tracers: effect of functionalization on physico-chemical properties, Nanoscale Res. Lett. 16 (2021) 1–16.
[23] M. Ježková, P. Jelínek, O. Marelja, D. Trunov, M. Jarošová, Z. Slouka, M. Šoóš, The preparation of mono- and multicomponent nanoparticle aggregates with layer-by-layer structure using emulsion templating method in microfluidics, Chem. Eng. Sci. 247 (2022) 117084.
[24] B.P. Pichon, O. Gerber, C. Lefevre, I. Florea, S. Fleutot, W. Baaziz, M. Pauly, M. Ohlmann, C. Ulhaq, O. Ersen, et al., Microstructural and magnetic investigations of wustite-spinel core-shell cubic-shaped nanoparticles, Chem. Mater. 23 (11) (2011) 2886–2900.
[25] X. Ding, L. Bao, J. Jiang, H. Gu, Colloidal synthesis of ultrathin γ-fe 2 o 3 nanoplates, RSC Adv. 4 (18) (2014) 9314–9320.
[26] E. Wetterskog, C.-W. Tai, J. Grins, L. Bergstrom, G. Salazar-Alvarez, Anomalous magnetic properties of nanoparticles arising from defect structures: topotaxial oxidation of fe1–x o— fe3- δo4 core— shell nanocubes to single-phase particles, ACS Nano 7 (8) (2013) 7132–7144.
[27] A. Demortiere, P. Panissod, B. Pichon, G. Pourroy, D. Guillon, B. Donnio, S. Bégin-Colin, Size-dependent properties of magnetic iron oxide nanocrystals, Nanoscale 3 (1) (2011) 225–232.
[28] Z. Chen, Size and shape controllable synthesis of monodisperse iron oxide nanoparticles by thermal decomposition of iron oleate complex, Synth. Reac. Inorg. Met.-Org. Nano-Met. Chem. 42 (7) (2012) 1040–1046.
[29] J. Mohapatra, A. Mitra, D. Bahadur, M. Aslam, Surface controlled synthesis of mfe 2 o 4 (m= mn, fe, co, ni and zn) nanoparticles and their magnetic characteristics, CrystEngComm 15 (3) (2013) 524–532.
[30] A. Roca, D. Niznansky, J. Poltierova-Vejpravova, B. Bittova, M. González-Fernández, C. Serna, M. Morales, Magnetite nanoparticles with no surface spin canting, J. Appl. Phys. 105 (11) (2009).
[31] A. Millan, A. Urtizberea, N. Silva, F. Palacio, V. Amaral, E. Snoeck, V. Serin, Surface effects in maghemite nanoparticles, J. Magn. Magn. Mater. 312 (1) (2007) L5–L9.
[32] M. Abdolrahimi, M. Vasilakaki, S. Slimani, N. Ntallis, G. Varvaro, S. Laureti, C. Meneghini, K.N. Trohidou, D. Fiorani, D. Peddis, Magnetism of nanoparticles: effect of the organic coating, Nanomaterials 11 (7) (2021) 1787.

[33] D. Peddis, C. Cannas, G. Piccaluga, E. Agostinelli, D. Fiorani, Spin-glass-like freezing and enhanced magnetization in ultra-small cofe2o4 nanoparticles, Nanotechnology 21 (12) (2010) 125705.
[34] L. Suber, P. Imperatori, A. Mari, G. Marchegiani, M.V. Mansilla, D. Fiorani, W. Plunkett, D. Rinaldi, C. Cannas, G. Ennas, et al., Thermal hysteresis of morin transition in hematite particles, Phys. Chem. Chem. Phys. 12 (26) (2010) 6984–6989.
[35] B. Gleich, J. Weizenecker, Tomographic imaging using the nonlinear response of magnetic particles, Nature 435 (7046) (2005) 1214–1217.
[36] S.J. Kemp, R.M. Ferguson, A.P. Khandhar, K.M. Krishnan, Monodisperse magnetite nanoparticles with nearly ideal saturation magnetization, RSC Adv. 6 (81) (2016) 77452–77464.
[37] N. Pérez, F. López-Calahorra, A. Labarta, X. Batlle, Reduction of iron by decarboxylation in the formation of magnetite nanoparticles, Phys. Chem. Chem. Phys. 13 (43) (2011) 19485–19489.
[38] S. Bandyopadhyay, M.K. Andersen, M.A.A. Alvi, A. Sharma, R. Raju, B.H. McDonagh, W.R. Glomm, Incorporation of fe@ au nanoparticles into multiresponsive pnipam-aac colloidal gels modulates drug uptake and release, Colloid Polym. Sci. 294 (2016) 1929–1942.
[39] A.M. de Oliveira, E. Jäger, A. Jäger, P. Stepánek, F.C. Giacomelli, Physicochemical aspects behind the size of biodegradable polymeric nanoparticles: a step forward, Colloids Surf. A, Physicochem. Eng. Asp. 436 (2013) 1092–1102.
[40] M. Beck-Broichsitter, J. Nicolas, P. Couvreur, Solvent selection causes remarkable shifts of the “ouzo region” for poly (lactide-co-glycolide) nanoparticles prepared by nanoprecipitation, Nanoscale 7 (20) (2015) 9215–9221.
[41] A.A. Öztürk, L.M. Banderas, M.D.C. Otero, E. Yenilmez, B. Şenel, Y. Yazan, Dexketoprofen trometamol-loaded poly-lactic-co-glycolic acid (plga) nanoparticles: preparation, in vitro characterization and cyctotoxity, Trop. J. Pharm. Res. 18 (1) (2019) 1–11.
[42] R.F. Pagels, J. Edelstein, C. Tang, R.K. Prud’homme, Controlling and predicting nanoparticle formation by block copolymer directed rapid precipitations, Nano Lett. 18 (2) (2018) 1139–1144.
[43] S.A. Love, M.A. Maurer-Jones, J.W. Thompson, Y.-S. Lin, C.L. Haynes, Assessing nanoparticle toxicity, Annu. Rev. Anal. Chem. 5 (2012) 181–205.
[44] J.R. Eidet, L. Pasovic, R. Maria, C.J. Jackson, T.P. Utheim, Objective assessment of changes in nuclear morphology and cell distribution following induction of apoptosis, Diagn. Pathol. 9 (2014) 1–9.
[45] A. Ashfaque, F. Hanif, S.U. Simjee, M.F. Bari, S. Faizi, S. Zehra, T. Mirza, S. Begum, L. Khan, Opuntiol inhibits growth and induces apoptosis in human glioblastoma cells by upregulating active caspase 3 expression, Asian Pac. J. Cancer Prev. 22 (11) (2021) 3607.
[46] J. Lee, J.-H. Lee, S.-Y. Lee, S.A. Park, J.H. Kim, D. Hwang, K.A. Kim, H.S. Kim, Antioxidant iron oxide nanoparticles: their biocompatibility and bioactive properties, Int. J. Mol. Sci. 24 (21) (2023) 15901.
[47] J. Sun, J. Walker, M. Beck-Broichsitter, S.P. Schwendeman, Characterization of commercial plgas by nmr spectroscopy, Drug Deliv. Transl. Res. 12 (3) (2022) 720–729.
[48] J. Garner, S. Skidmore, H. Park, K. Park, S. Choi, Y. Wang, A protocol for assay of poly (lactide-co-glycolide) in clinical products, International journal of pharmaceutics 495 (1) (2015) 87–92.